**Astronomy
&
Astrophysics**

MUSE observations towards the lensing cluster A2744: Intersection between the LBG and LAE populations at *z* ~ 3–7

G. de La Vieuville[1], R. Pelló[2,1], J. Richard[3], G. Mahler[4,5], L. Lévêque[1], F. E. Bauer[6,7,8], D. J. Lagattuta[3], J. Blaizot[3], T. Contini[1], L. Guaita[6], H. Kusakabe[9], N. Laporte[1,10,11], J. Martinez[3], M. V. Maseda[12], D. Schaerer[9], K. B. Schmidt[13], and A. Verhamme[9]

[1] Institut de Recherche en Astrophysique et Planétologie (IRAP), Université de Toulouse, CNRS, UPS, CNES, 14 Av. Edouard Belin, 31400 Toulouse, France
e-mail: gdelavieuvil@irap.omp.eu
[2] Aix Marseille Université, CNRS, CNES, LAM (Laboratoire d'Astrophysique de Marseille), UMR 7326, 13388 Marseille, France
e-mail: roser.pello@lam.fr
[3] Univ Lyon, Univ Lyon1, Ens de Lyon, CNRS, Centre de Recherche Astrophysique de Lyon (CRAL) UMR5574, 69230 Saint-Genis-Laval, France
[4] Department of Astronomy, University of Michigan, 1085 S. University Ave., Ann Arbor, MI 48109, USA
[5] Department of Physics and Astronomy, University College London, Gower Street, London WC1E 6BT, UK
[6] Instituto de Astrofísica and Centro de Astroingeniería, Facultad de Física, Pontificia Universidad Católica de Chile, Casilla 306, Santiago 22, Chile
[7] Space Science Institute, 4750 Walnut Street, Suite 205, Boulder, Colorado 80301, USA
[8] Millenium Institute of Astrophysics (MAS), Nuncio Monseñor Sótero Sanz 100, Providencia, Santiago, Chile
[9] Observatoire de Genève, Université de Genève, 51 Ch. des Maillettes, 1290 Versoix, Switzerland
[10] Cavendish Laboratory, University of Cambridge, 19 JJ Thomson Avenue, Cambridge CB3 0HE, UK
[11] Kavli Institute for Cosmology, University of Cambridge, Madingley Road, Cambridge CB3 0HA, UK
[12] Leiden Observatory, Leiden University, PO Box 9513, 2300 Leiden, RA, The Netherlands
[13] Leibniz-Institut für Astrophysik Potsdam (AIP), An der Sternwarte 16, 14482 Potsdam,, Germany

ABSTRACT

We present a study of the intersection between the populations of star forming galaxies selected as either Lyman break galaxies (LBGs) or Lyman-alpha emitters (LAEs) in the redshift range 2.9−6.7 and within the same volume of universe sampled by the Multi-Unit Spectroscopic Explorer (MUSE) behind the *Hubble* Frontier Fields lensing cluster A2744. We define three samples of star-forming galaxies: LBG galaxies with an LAE counterpart (92 galaxies), LBG galaxies without an LAE counterpart (408 galaxies), and LAE galaxies without an LBG counterpart (46 galaxies). All these galaxies are intrinsically faint because of the lensing nature of the sample ($M_{1500} \geq -20.5$). The fraction of LAEs among all selected star-forming galaxies increases with redshift up to $z \sim 6$ and decreases for higher redshifts, in agreement with previous findings. The evolution of LAE/LBG populations with UV magnitude and Lyα luminosity shows that the LAE selection is able to identify intrinsically UV faint galaxies with $M_{1500} \geq -15$ that are typically missed in the deepest lensing photometric surveys. The LBG population seems to fairly represent the total population of star-forming galaxies down to $M_{1500} \sim -15$. Galaxies with $M_{1500} < -17$ tend to have $SFR_{Ly\alpha} < SFR_{uv}$, whereas the opposite trend is observed within our sample for faint galaxies with $M_{1500} > -17$, including galaxies only detected by their Lyα emission, with a large scatter. These trends, previously observed in other samples of star-forming galaxies at high-*z*, are seen here for very faint $M_{1500} \sim -15$ galaxies; that is, much fainter than in previous studies. The present results show no clear evidence for an intrinsic difference between the properties of the two populations selected as LBG and/or LAE. The observed trends could be explained by a combination of several phenomena, like the existence of different star-formation regimes, the dust content, the relative distribution and morphology of dust and stars, or the stellar populations.

Key words. gravitational lensing: strong – galaxies: high-redshift – dark ages, reionization, first stars

1. Introduction

Intrinsically faint star-forming galaxies (SFGs) are presently considered as the main sources responsible for cosmic reionization. Ultra-deep photometry obtained using the *Hubble* Space Telescope (HST on blank fields combined with ground-based photometry and spectroscopy has fundamentally improved our knowledge of the galaxy UV luminosity function (LF) up to $z \sim 10$ (see e.g., Bouwens et al. 2004, 2015a; McLure et al. 2013; Finkelstein et al. 2015 and the references therein). The integration of the UV LF is used to derive the evolution of the cos-

mic star-formation density and the density of ionizing radiation (usually assuming a constant star-formation rate), with the two key parameters being the slope of the faint end of the LF and the faint-end integration limit (see e.g., Bouwens et al. 2015b). Up to $z \sim 7$, current observations reach as deep as $M_{1500} \sim -17$ in blank fields, which is about three magnitudes brighter than the faint-end UV luminosity limit needed to reionize the universe at $z \sim 6-7$. Using lensing clusters as gravitational telescopes makes it possible to reach $M_{1500} \sim -15$ at $z \sim 7$, thereby improving our constraints on the contribution of SFGs to reionization (see e.g., the work done in Atek et al. 2015 and

Livermore et al. 2017 using data from the *Hubble* Frontier Fields (HFF) project; Lotz et al. 2017).

However, the ability of SFG to reionize the universe depends not only on the faint-end slope of the UV LF (and its actual shape) and the faint-end integration limit, but also on the escape fraction of ionizing radiation. In addition, most samples used for this exercise, either in blank fields or in lensing fields, are photometrically selected and have few if any spectroscopic redshifts available. The interrelation between the different SFG populations, which are selected as Lyman-break galaxies (LBGs) or Lyman-alpha emitters (LAEs), has been a popular topic for many years, both from observational and theoretical points of view (see e.g., Nagamine et al. 2010; Pentericci et al. 2011; Shapley 2011; Stark et al. 2011; Dayal & Ferrara 2012; Erb et al. 2014; Orsi et al. 2014; Tilvi et al. 2014; Schenker et al. 2014; Garel et al. 2016; De Barros et al. 2017; Caruana et al. 2018; Arrabal Haro et al. 2018).

The same holds for the relative escape fractions of Lyα and UV photons (i.e., the ability of observed quantities such as Lyα and rest-frame UV fluxes to trace the ionizing radiation; noted hereafter $f_{Ly\alpha}$ and f_{uv}; see e.g., Hayes et al. 2015; Steidel et al. 2018 and the references therein).

Nevertheless, observations of LBGs and LAEs are rarely carried out in the same volume of universe because of observational limitations. Recent pioneering studies have started to address this issue in blank fields, such as for example Arrabal Haro et al. (2018) using the SHARDS survey of the GOODS-N field which is a deep-imaging survey using 25 medium band filters, or Inami et al. (2017) Hashimoto et al. (2017), Maseda et al. (2018), and Kusakabe et al. (2020), all based on ultra-deep integral field units (IFU) data for the *Hubble* Ultra Deep Field (HUDF) from MUSE (the Multi-Unit Spectroscopic Explorer; Bacon et al. 2010, 2017).

In this paper, we investigate the intersection between the populations of SFGs selected as LBGs and LAEs in the range $2.9 < z < 6.7$ within the same volume of universe sampled by MUSE behind the HFF lensing cluster Abell 2744 (hereafter A2744). For the first time, such a combined survey is performed behind a lensing cluster, using the deepest images available from the HFF. Taking advantage of the magnification provided by the lensing cluster, the survey reaches an average depth of $M_{1500} \sim -15$ and probes galaxies as faint as $M_{1500} \sim -12$ in some areas, and Lyα luminosities in the range $40 \lesssim \log(L_{Ly\alpha}) \lesssim 43$. We investigate the prevalence of Lyα emission among the faintest LBG population ($M_{1500} > -20.25$), as well as the relationship between Lyα and UV luminosity. Hereafter the term LBG is used to refer to galaxies identified by their UV continuum using either the classical color–color diagrams (see e.g., Steidel et al. 2003; Oesch et al. 2007; Bouwens et al. 2015a or photometric redshifts (see e.g., McLure et al. 2009; Pelló et al. 2018). In Sect. 2 we briefly describe the relevant MUSE and HFF data available for this study. Section 3 presents the selection of LBG and LAE samples at $z \sim 3-7$ behind A2744. The results on the intersection of LBG and LAE populations are presented and discussed in Sect. 4. Conclusions are given in Sect. 5. The cosmology adopted throughout this paper is $\Omega_\Lambda = 0.7$, $\Omega_m = 0.3$ and $H_0 = 70$ km s^{-1} Mpc^{-1} and all magnitudes are given in the AB system (Oke & Gunn 1983).

2. MUSE and HFF data of A2744

MUSE integral-field observations of A2744 were carried out as part of the MUSE Guaranteed Time Observing (GTO) program on lensing clusters (GTO Program 094.A-0115; PI: Richard;

see Mahler et al. 2018; de La Vieuville et al. 2019 for additional information). The field observed was a 2×2 MUSE mosaic covering the entire multiple-image area, with exposure times ranging between 3.5 and 5 hours per pointing, plus a central pointing with two additional hours of exposure centered at α=00:14:20.95 δ=-30:23:53.9 (J2000). All details regarding MUSE data reduction, the source-detection process, and mass model construction can be found in Mahler et al. (2018). Throughout this study we use the gold mass model presented in Table 4 of Mahler et al. (2018) which has an average RMS of multiple images in the image plane of 0.67″. The MUSE catalog includes 171 LAEs[1] before multiple image removal, with redshifts in the range $2.9 < z < 6.7$. All LAEs were detected with Muselet[2], a detection software for emission lines in MUSE cubes. Table 1 summarizes the effective lens-corrected volume surveyed by the MUSE observations behind A2744. The detection fluxes of the LAEs are measured with SExtractor (Bertin & Arnouts 1996) using the `MAG_AUTO` segmentation on Lyα narrow-band (NB) images. These NB images are continuum subtracted, and their spectral width is manually adjusted to the spectral extent of each LAE to ensure the best recovery of the total Lyα flux. The automated segmentation is efficient in dealing with a wide variety of spatial profiles, including high distortion induced by lensing. All technical details regarding the LAE extraction method including some examples can be found in Sect. 3.2 of de La Vieuville et al. (2019).

The selection of LBGs in this field is based on the HFF observations of A2744 (ID: 13495, P.I: J. Lotz). Seven filters are available for *Hubble* Space Telescope data, three from the Advanced Camera for Surveys (ACS: F435W, F606W, F814W), and four from the Wide Field Camera 3 (WFC3: F105W, F125W, F140W, and F160W). In this study we use self-calibrated data provided by STScI (version v1.0 for WFC3 and v1.0-epoch2 for ACS) with a pixel size of 60 mas. The full MUSE mosaic is contained within all of these seven HFF bands. We used the photometric catalog released by Astrodeep (Merlin et al. 2016; Castellano et al. 2016), which also includes imaging from VLT/Hawk-I K-band and the first two *Spitzer*/IRAC bands. For each of the seven HST filters, both the intra-cluster light (ICL) and bright-cluster galaxies (BCGs) were modeled and subtracted. The photometry was measured on these processed images with SExtractor (Bertin & Arnouts 1996) with PSF matching techniques using high-spatial-resolution images as priors for the source segmentation. The complete procedure is detailed in Merlin et al. (2016). The complete catalog has 3587 entries for the entire A2744 lensing field, of which 2596 are detected in the F160W image, a further 976 are detected in a weighted stack of F105W, F125W, F140W, and F160W and undetected in F160W alone, and 15 are BCGs. We note that the Astrodeep catalog is near-infrared(NIR)-selected by construction, and this fact could have some implications on the subsequent results.

Before any comparison with the MUSE source catalog, the entire Astrodeep catalog was filtered to remove untrustworthy photometry points and/or sources. Because VLT/Hawk-I, IRAC 1, and IRAC 2 have larger PSFs than the HST filters, the photometry computed in these three bands is more often contaminated by nearby galaxies. Following the flags given in the catalog, all photometric entries likely to be affected by this effect (indicated by flag COVMAX; see Merlin et al. (2016)) were given an upper detection limit in these filters when computing photometric

---

[1] Publicly available at http://muse-vlt.eu/science/a2744/
[2] Muselet is part of the python MPDAF package (Piqueras et al. 2017)

redshifts. We also removed 220 sources flagged as likely residuals of the foreground subtraction (SEXFLAG > 16 and VISFLAG > 1). Finally, the catalog was cut to the exact MUSE field-of-view (FoV), leading to a final selection of 2666 sources detected in the Astrodeep catalog within the MUSE mosaic.

In order to build a single coherent catalog, a cross match was performed between the remaining 2666 Astrodeep sources and the 171 LAEs of the MUSE catalog using a matching radius of $r = 0.8''$ (4 MUSE pixels). In case several entries are pointing towards the same source, only the closest match is kept. The difference in morphology between the UV and Lyα emission (see e.g., Leclercq et al. 2017; Wisotzki et al. 2018) and the distortions induced by lensing are likely to be the dominant causes of mismatch. For this reason, all LAEs and their closest Astrodeep counterpart were manually inspected to confirm or reject the match. In the case of multiple-image systems, it is always possible to select the least ambiguous image of the system when assembling the final sample (see below). At the end of the matching process, the merged catalog contains 2724 galaxies of which 113 are seen in both the MUSE and Astrodeep catalogs, and 58 are LAEs with no detected UV counterpart in the Astrodeep catalog.

3. Selection of LBG and LAE galaxies at $z \sim 2.9–6.7$

Two different methods were used to select LBGs in this field among the sources detected by Astrodeep in the MUSE FoV: the usual three-band dropout technique applied to HFF data, and a method based on pure photometric redshifts and probability distributions. For the dropout (two-color) technique, we adopted the same criteria as proposed by Bouwens et al. (2015a) for the selection of galaxies at $z \sim 3.8, 4.9, 5.9$, and 6.8. Photometric redshifts and redshift probability distribution (noted $P(z)$) were computed with the code *New–Hyperz*[3], which was originally developed by Bolzonella et al. (2000) based on the fitting of the photometric spectral energy distributions (SED) of galaxies. The input Astrodeep catalog presented in Sect. 2 also includes photometric redshifts. However, a new evaluation of the photometric redshifts is carried out here in order to preserve the consistency of the fit obtained for the different parameters used in this study.

Photometric redshifts with *New–Hyperz* were computed in the range $z = [0, 8]$. The template library used in this study includes 14 templates: eight evolutionary synthetic SEDs from the Bruzual and Charlot code (Bruzual & Charlot 2003), with Chabrier initial mass function (IMF; see Chabrier 2003) and solar metallicity; a set of four empirical SEDs compiled by Coleman et al. (1980); and two starburst galaxies from the Kinney et al. (1996) library. Internal extinction is considered as a free parameter following the Calzetti et al. (2000) extinction law, with A_V ranging between 0 and 1.0 magnitudes, and no prior in luminosity. At this stage, galaxies with photometric redshifts higher than $z \geq 2.9$ and integrated probability distributions $P(z > 2.9) > 60\%$ were selected as LBGs. In all cases, an S/N higher than 3σ was required at this stage in at least one of the filters encompassing the rest-frame UV. The quality of photometric redshifts is assessed by directly comparing the results for the galaxies with known spectroscopic redshifts in the LBG sample. Outliers are defined as sources with $|z_{\text{spec}} - z_{\text{phot}}| > 0.15(1 + z_{\text{spec}})$. The average accuracy reached excluding outliers is $\Delta z/(1 + z) = -0.011 \pm 0.053$, with a median at $\Delta z/(1 + z) = 0.001$. As seen in Fig. 1, the vast majority of galaxies with poor photometric redshifts have $m(\text{F125W}) \geq 28$ (or an $S/N < 5$ in

[3] http://userpages.irap.omp.eu/~rpello/newhyperz/
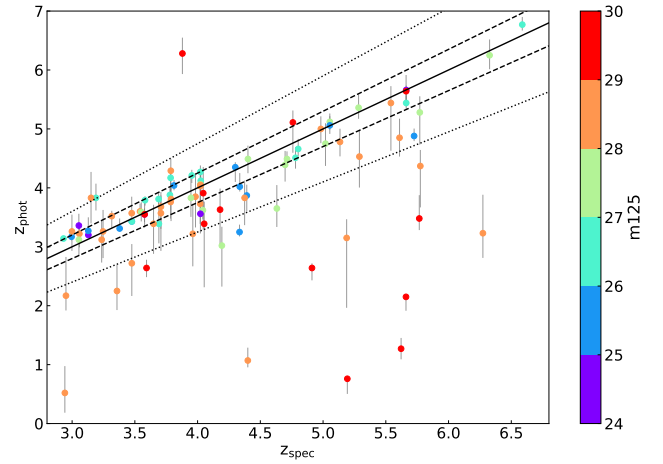
Fig. 1. Comparison between photometric and spectroscopic redshifts for galaxies spectroscopically confirmed at $z \sim 3-7$. Long-dashed and dashed lines display the locus of $z_{\text{phot}} = z_{\text{spec}} \pm 0.05(1 + z)$ and $\pm 0.15(1 + z)$ respectively, and the solid black line is the one-to-one relation. Colors encode the observed magnitudes in the F125W filter, showing that the vast majority of galaxies with poor photometric redshifts have $m(\text{F125W}) \geq 28$.

this filter). It is also worth noting that good photometric redshifts could be obtained for galaxies with $z \gtrsim 2.9$, which fully covers the redshift domain where the Lyα line can be detected by MUSE.

Given the trends found for the quality of photometric redshifts computed with *New–Hyperz*, an S/N higher than 5 was requested in at least one of the seven HST filters for sources without spectroscopic redshifts. For galaxies with a spectroscopic confirmation, no S/N criterion was imposed. This means that 9 of the 92 galaxies spectroscopically selected have an S/N lower than 5, typically ranging between 3 and 5 in several filters, a small enough fraction to preserve the results of the subsequent analysis (see Sect. 4). Using this blind photometric redshift procedure, and the S/N criterion, 536 galaxies were selected as LBGs.

For comparison, the three-band dropout technique selects 383 objects, all of them included within the sample obtained with blind photometric redshifts, with only ten exceptions. Inspection of these ten objects revealed that they have either unreliable photometric points resulting in poorly constrained or undefined photometric redshift, or that they have $z_{\text{phot}} \sim 2.9$ with a large part of their $P(z)$ under the $z = 2.9$ threshold, therefore failing the $P(z > 2.9) \geq 60\%$ criterion.

Because we want to be as inclusive as possible in our selection, all galaxies selected for their UV continuum and photometric redshift as described above are considered in the rest of this study. For the sake of simplicity, we continue using the term "LBG" to refer to this photo-z sample. Furthermore, even though the presence of a break is not strictly required in our selection, it remains the main feature picked up by *New–Hyperz* to compute the photometric redshift for most of our galaxies.

Finally, all images were inspected to identify multiple systems. For LAEs, a robust identification of multiple systems is already provided in the MUSE catalog. For LBGs with no LAE counterparts, the identification of multiple system is done using LENSTOOL (Kneib et al. 1996; Jullo et al. 2007; Jullo & Kneib 2009) and the predictions of the mass models presented in Mahler et al. (2018). Therefore, for all identified multiple image systems (both LAEs and LBGs) we only keep one source counterpart, to avoid including the same object several times in
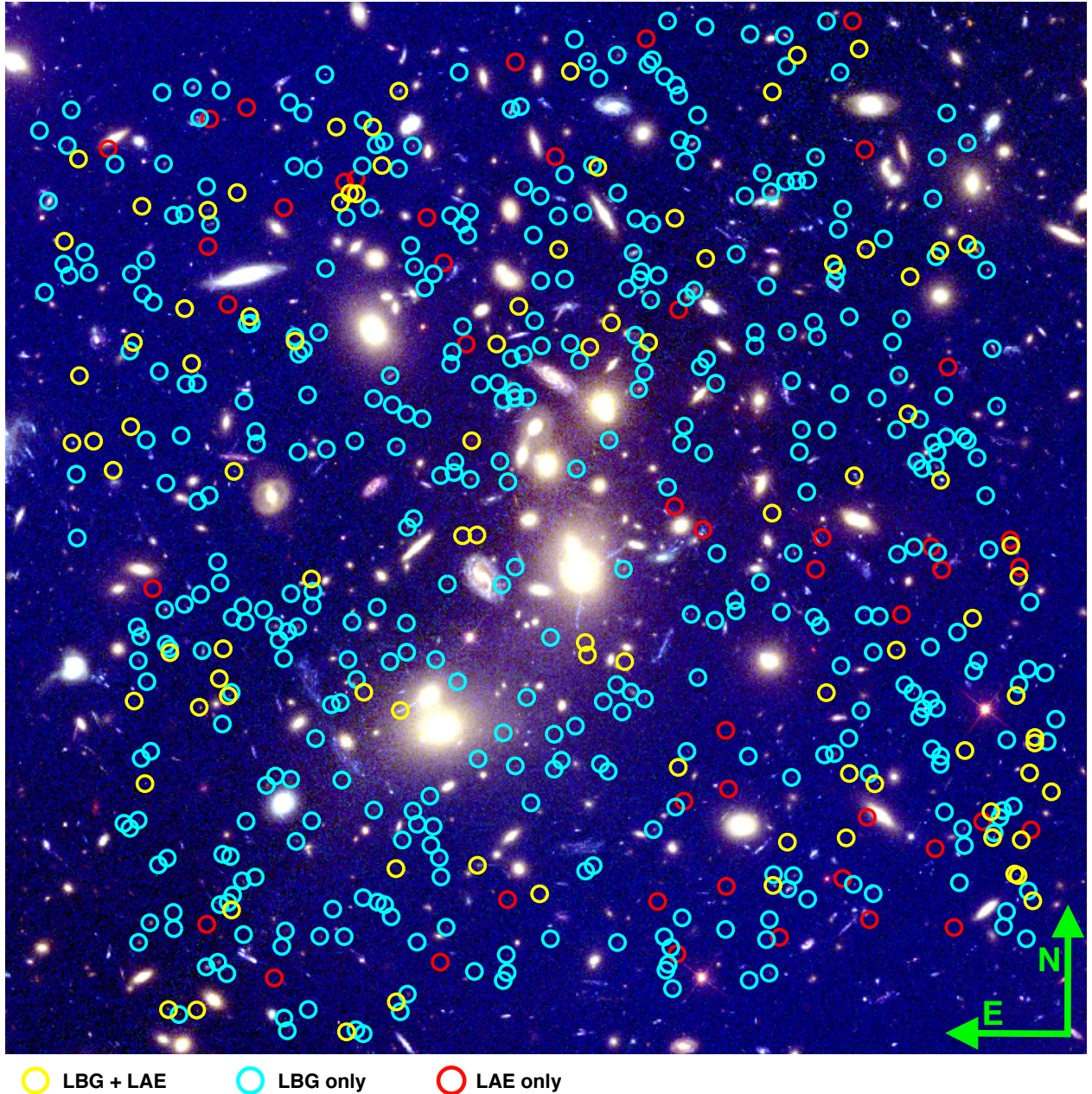
Fig. 2. False-color image of A2744 showing the area covered by the MUSE observations, which was obtained by combining the following HFF filters: F435W (blue), F606W (green), and F814W (red). The different populations selected in this field at $2.9 < z < 6.7$ are displayed as follows: LBGs without an LAE counterpart in cyan (408), LBGs with an LAE counterpart in yellow (92), and LAEs without an LBG counterpart in red (58). Circles are 1.5″ in diameter.

our analysis. In case one LAE image of a system matches with a UV counterpart and the other(s) do not, the one with the UV counterpart is kept.

## 4. The intersection between LBG and LAE populations

The following samples are defined in the MUSE field behind A2744 after the selection process and multiple image removal presented in Sect. 3:

– Sample 1: LBG galaxies with Lyα emission (hereafter LBG + LAE) This sample contains 92 galaxies.
– Sample 2: LBG galaxies without Lyα emission, including 408 galaxies selected by their UV rest-frame continuum.

– Sample 3: LAE galaxies without an LBG counterpart. This sample contains 46 galaxies.

Figure 2 displays the different populations selected in this field overlaid on a false color image of A2744. In practice, the matching between the centroids of LBG and LAE galaxies is usually better than 0.1″ (average value in the LBG + LAE sample). In the selection above, one concern is that some galaxies would be seen as pure LAEs because their Lyα emission can be detected by MUSE overlaid on some bright foreground galaxy, whereas their UV continuum cannot be detected. Such identification of pure LAEs would be completely artificial as it would not be representative of the intrinsic properties of the source but only of the foreground contamination. The risk has been limited by the selection of the most representative image in multiple-imaged
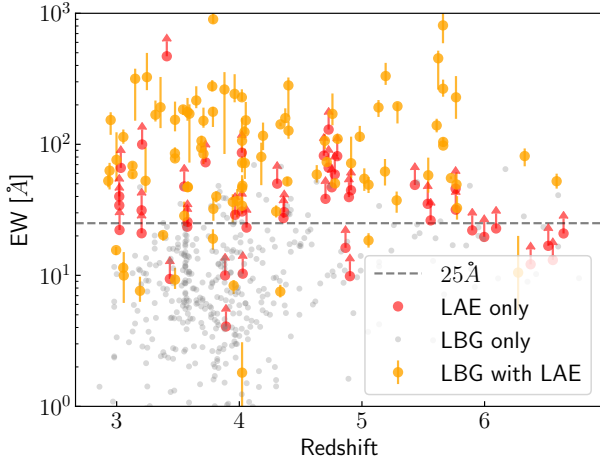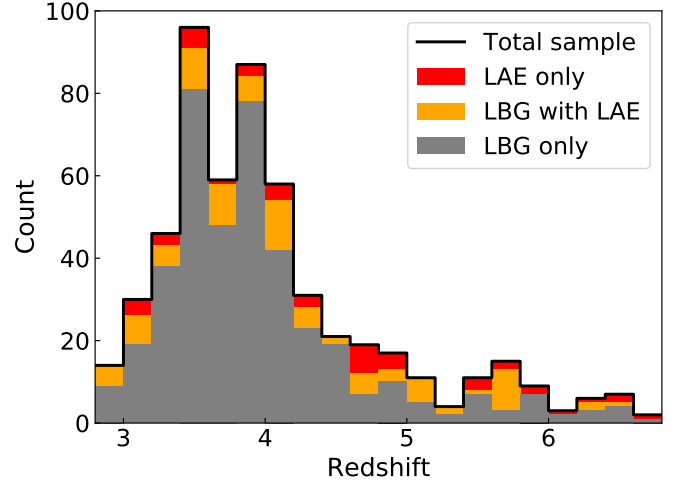
Fig. 3. Redshift distribution of the rest-frame EW for Lyα emission in the three samples. For the LBGs without an LAE counterpart in gray, the values are upper limits and the error bars have been omitted for clarity. The dashed horizontal line corresponds to EW$_{\mathrm{Ly}\alpha}$ =25 Å.

Fig. 4. Redshift distribution of the three samples defined in this study. See text in Sect. 3 for more details on the selection of the three samples.

systems (when possible), as explained in Sect. 3. Indeed, as displayed in Fig. 2, none of the pure LAEs (red circles) fall on top of a bright foreground galaxy that would prevent the detection of an underlying UV continuum.

In order to determine the values of the UV continuum, in particular the continuum emission at the wavelength of the Lyα line (hereafter referred to as the Lyα continuum) and the absolute magnitudes M_{1500}, a SED-fitting process was adopted using star-forming and young star-burst templates (age <1 Gyr) extracted form the Starbursts99 library (Leitherer et al. 1999). To estimate the uncertainty on both the Lyα continuum and M_{1500}, we performed Monte Carlo (MC) iterations by drawing the photometry points within their error bars and iteration of the SED-fitting process. In practice, for sources without spectroscopic redshifts, *New–Hyperz* was run twice: the first time to determine the best photometric solution and $P(z)$ as described in Sect. 3, and a second time using the results of the first run to fix the best-fit redshift and perform the MC iterations. When comparing the blind photo-z obtained during the first pass to the one derived with the Starbursts99 library of templates (leaving the full redshift range free), they are found to be in full agreement for all galaxies selected as LBGs. For sources with spectroscopic redshifts, the redshift was fixed to the spectroscopic value during MC iterations.

For the galaxies selected as both LAEs and LBGs, it is possible to compute their EW$_{\mathrm{Ly}\alpha}$ using their detection flux and the Lyα continuum measured from the best-fit SEDs. For galaxies selected as pure LAEs and pure LBGs, only lower and upper limits of the EW$_{\mathrm{Ly}\alpha}$ can be determined respectively. The distribution of the rest frame EW$_{\mathrm{Ly}\alpha}$ with redshift for the three samples is presented in Fig. 3. As the magnification affects both the continuum and the Lyα emission in the same way, no additional correction is needed. For the LBG with no LAE counterpart (Sample 2), the upper limit of their Lyα emission is assumed to be a constant flux of F(Lyα) = 1×10^{-18} erg^{-1} s^{-1} cm^{-2}. In the following, the reader should keep in mind that this is a somewhat arbitrary estimate corresponding to the flux limit above which more than 90% of the LAEs detected behind A2744 are found. A flux value ranging between 2 and 5×10^{-18} erg^{-1} s^{-1} cm^{-2}, depending on the spatial and spectral profile of the source, could be used to secure a detection limit close to 100% completeness (see Fig. 9 in de La Vieuville et al. 2019). For galaxies selected as pure LAEs

in Sample 3, a limiting flux for the Lyα continuum and the corresponding apparent magnitude m_{1500} were obtained for each object based on the noise of the sky background measured on the top of the area where the Lyα emission was detected, using the photometric images encompassing these wavelengths. As Sample 3 LAEs are relatively compact, a compact PSF-dominated morphology was also assumed for these galaxies in the continuum, with a maximum of 2σ above the local sky background. This procedure allows us to take into account the different detection conditions for the continuum affecting these galaxies, in particular close to the cluster core.

### 4.1. Evolution with redshift

Redshift histograms for the three samples considered in this study are shown stacked on top of each other in Fig. 4. Table 1 displays the same information but with the redshift bins used in de La Vieuville et al. (2019) for the computation of the LAE LF. As seen in the table and figure, the proportion of LAEs (i.e., LBG + LAE and LAE only) among SFGs increases with redshift despite the fact that these are the deepest images available in the HFF survey. We acknowledge that these values depend on the relative depth of the photometric and spectroscopic surveys, and as such they only indicate an observed trend for our data set.

Using Samples 1 and 2 (LAE + LBG and LBG only) it is also possible to compute the fraction of LAEs with EW$_{\mathrm{Ly}\alpha} > 25$ Å among our UV-selected sample, noted X$_{\mathrm{LAE}}$. This fraction, used to express the prevalence of LAEs among the LBG population, is often divided into two populations: galaxies with $M_{1500} < -20.25$ and galaxies with $M_{1500} > -20.25$ (see e.g., Stark et al. 2011; Pentericci et al. 2011; Arrabal Haro et al. 2018). Because of the lensing nature of the present sample, it is mostly dominated by faint galaxies and 98% of the sample falls within the $M_{1500} > -20.25$ domain. The limit EW$_{\mathrm{Ly}\alpha} = 25$ Å is shown in Fig. 3 and again most of our LAE sample falls above that limit. The LAE fraction is computed from Samples 1 and 2 with the cuts in both EW$_{\mathrm{Ly}\alpha}$ and UV magnitude described above, that is, using the upper limits for pure LBGs (Sample 2) at face values. The results are presented with and without completeness correction for the LAE selection in Fig. 5 using the following redshift bins: $2.9 < z < 4.0$, $4.0 < z < 5.0$, $5.0 < z < 6.0$, and $6.0 < z < 6.7$. This binning was adopted to reach a sufficient sample size in each bin – for statistical purposes – and to

Table 1. Interrelation between the LAE and LBG populations.

	$2.9 \leq z \leq 6.7$	$2.9 \leq z \leq 4.0$	$4.0 \leq z \leq 5.0$	$5.0 \leq z \leq 6.7$
Effective volume (Mpc³)	13 361	4546	3638	5177
Sample 1: LBG with LAE	**92 ± 9.6**	**43 ± 6.6**	**27 ± 5.2**	**22 ± 4.7**
	16.9 ± 1.7%	13.2 ± 2.0%	18.0 ± 3.5%	32.8 ± 7.0%
Sample 2: LBG only	**406 ± 20.1**	**286 ± 16.9**	**105 ± 10.2**	**33 ± 5.7**
	74.6 ± 3.7%	81.9 ± 5.2%	70.0 ± 6.8%	49.2 ± 8.5%
Sample 3: LAE only	**46 ± 6.8**	**16 ± 4.0**	**18 ± 4.2**	**12 ± 3.5**
	8.4 ± 1.2%	4.9 ± 1.2%	12.0 ± 2.8%	17.9 ± 5.2%
Total	**544 ± 23.3**	**327 ± 18.1**	**150 ± 12.2**	**67 ± 8.2**

Notes. Numbers in boldface are absolute number of detections, and uncertainties correspond to the Poissonian error count.
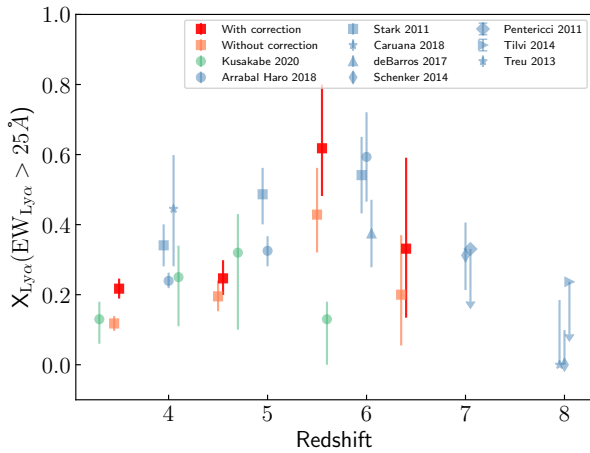
Fig. 5. Fraction of LAEs with $EW_{Ly\alpha} > 25$ Å among the UV-selected galaxies with $M_{1500} > -20.25$. This fraction is computed from galaxies in Samples 1 and 2, and compared to other similar values in the literature (see Sect. 4.1 for more details). For clarity, a small redshift offset is applied to the points centered on the same redshift value.

easily compare with previous results, in particular around the $z \sim 6$ epoch.

The completeness of the LAE selection is determined using the method presented in de La Vieuville et al. (2019). The individual maximum covolume of detection for each LAE is computed in the A2744 cube and is noted $V_{max,i}$. This computation is done in the source plane, simulating the detectability of individual LAEs across numerous spectral layers (or monochromatic layers) and restricting the computation to the spatial areas where the magnification field is high enough to allow the detection of the LAE. An additional correction noted C_i is considered to account for the fact that the LAE does not have a 100% chance of being detected on its own spectral layer because of the random variation of noise across the spatial dimension of the layer. This C_i takes values in the range 0–1 and is computed on the detection layer of individual LAEs by injecting their own detection profile multiple times across the FoV and trying to recover it. All the technical details related to the computation of $V_{max,i}$ and C_i can be found in de La Vieuville et al. (2019).

The factor $1/C_i V_{max,i}$ gives a numerical density for one LAE. To compute a correction from this numerical density, two additional quantities are introduced: the limit magnification noted $\mu_{lim,i}$ and $V(>\mu)$. The limit magnification is the magnification value under which the S/N of a given LAE drops below one, and represents the minimum value of magnification for a specific

LAE to be detected. The second quantity, $V(>\mu)$, is the volume of observation explored above a given magnification, computed from the source plane. For each LAE, the corrected contribution of $1/C_i V_{max,i}$ to X_{LAE} is given by:

$$N(LAE)_{corr,i} = \frac{V(>\mu_{lim,i})}{C_i V_{max,i}}. \tag{1}$$

The term $V(> \mu_{lim,i})$ is the volume of observations above a given amplification (i.e., neglecting the effects of the spectral variations of noise across the layers of the cube) and is used to normalize the intrinsic numerical density of the LAE. The aim of such a normalization is based on the fact that the background volume explored varies strongly depending on the magnification regime considered as faint sources can only be detected within the highly magnified regions. The correction of all LAEs with $N(LAE_{corr,i}) \geq\geq 10$ is neglected as it is estimated as untrustworthy. For a given UV-selected population, assumed to be complete, the fraction X_{LAE} is computed for two cases, the corrected and the uncorrected population of LAEs. Only Poissonian uncertainties are considered for the error propagation affecting X_{LAE}.

In Fig. 5, the present results are compared to the ones derived by previous authors for $M_{1500} > -20.25$, namely those of Stark et al. (2011), Pentericci et al. (2011), Treu et al. (2013), Schenker et al. (2014), Tilvi et al. (2014), De Barros et al. (2017), and Arrabal Haro et al. (2018), keeping in mind that the definition of the M_{1500} range in the literature is not identical for the different authors; it is $-20.25 < M_{1500} < -18.75$ for Stark et al. (2011) and Pentericci et al. (2011), whereas it is $M_{1500} > -20.25$ in this work and for Treu et al. (2013), Schenker et al. (2014), Tilvi et al. (2014), De Barros et al. (2017), Caruana et al. (2018), and Arrabal Haro et al. (2018). As expected, the present determination of X_{LAE} increases from $z = 3.5$ to $z = 5.5$ and drops for $z > 6$, which can be interpreted as an increase in the neutral fraction of hydrogen. Our corrected points are most consistent with the determination of X_{LAE} from Arrabal Haro et al. (2018). Even though all of our corrected points are roughly consistent to 1σ level with the other values from the literature, it appears that the two lower redshift points tend to be below previous estimates. Several factors may explain this observed trend.

Because of the lensing nature of the present sample, the volume probed is small, only ~13 360 Mpc³ are explored in the range $2.9 < z < 6.7$, and the cosmic variance has therefore a high impact on the observed statistics. This additional uncertainty is not shown in the error bars.

There is clearly a difference in the selection processes with respect to previous studies. Here we use both broad-band photometry and IFU observations. The combination of these two methods ensures that we are as unbiased as possible in both
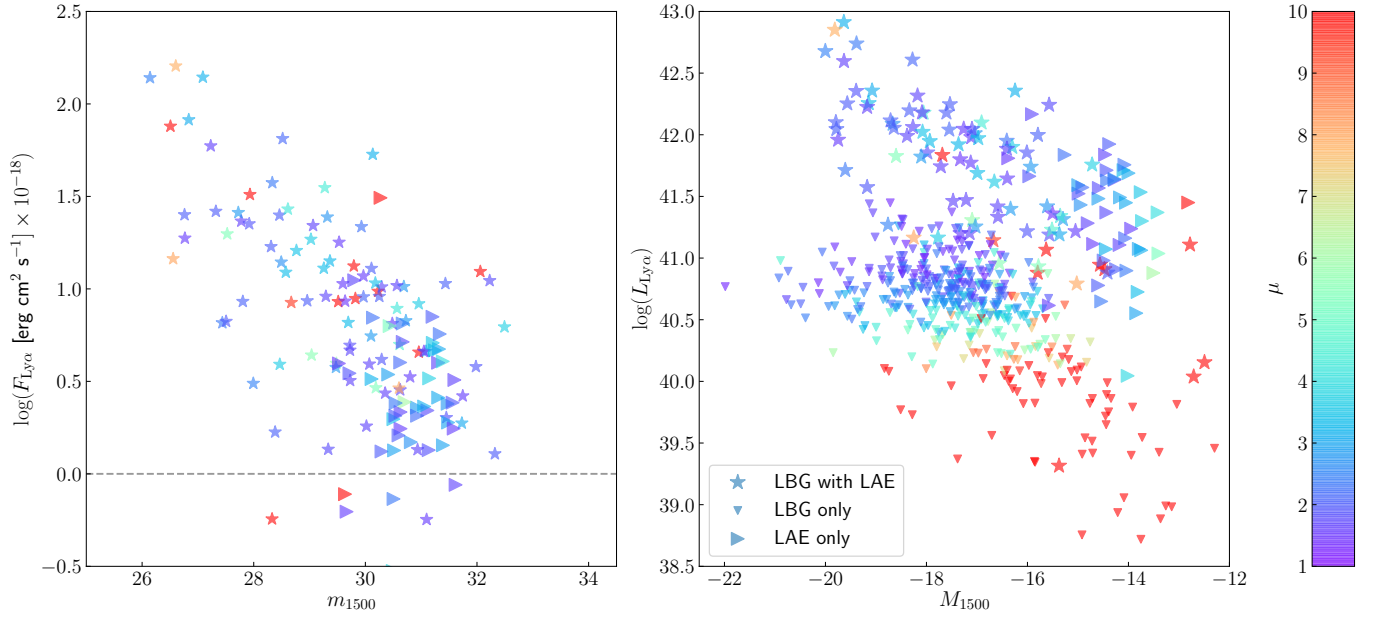
Fig. 6. Distribution of the different populations of SFG in their observed and derived properties, showing the magnification μ affecting each galaxy in a color-coded value (see color scale on the right). *Left panel*: observed Lyα flux versus apparent magnitude m_{1500}, without any correction for magnification, for Samples 1 and 3. The m_{1500} value was recomputed based on the SED of each galaxy in Sample 1; for Sample 3, it is the limiting magnitude for each source as described in Sect. 4. The limiting Lyα flux assigned to all galaxies in Sample 2 is shown by a gray dashed line. *Right panel*: Lyman α luminosity versus absolute UV magnitude M_{1500} after correction for magnification μ. No correction for dust extinction was applied. The effect of magnification in spreading the distribution of galaxies towards the faintest values is clearly seen in this figure.

the LBG and LAE selection in the same volume, range of magnitude, and Lyα luminosity. All LAEs with a detected continuum are included in Sample 1, even if this detected continuum has a lower S/N that would not have allowed it to pass the photometric selection required for the pure LBGs of Sample 2 (this effect only accounts for ~10% of Sample 1). On one hand, two-step surveys based on LAEs spectroscopically identified among photometrically pre-selected LBG populations are likely missing LAEs with the faintest continuum counterparts or exhibiting extended and/or ex-centered Lyα emission. On the other hand, Lyα emission is also likely to affect broad-band photometry used in the LBG pre-selection as well as the UV detection limit, as discussed in Kusakabe et al. (2020). On the contrary, Arrabal Haro et al. (2018) used the 25 medium bands of the SHARDS survey to select both the LBG and LAE populations. These observations have an average depth of $m = 26.5-29$ magnitude and an average spectral resolution of $R \sim 50$. They are therefore mostly sensitive to UV-brighter galaxies and higher EW$_{Ly\alpha}$, but are able to probe a much larger area. In this regard, this present study is complementary to their findings.

Finally, we get ~40% more objects using a photo-z selection compared to a more traditional color–color selection (see beginning of Sect. 3). This selection effect tends to lower our measurement of X$_{LAE}$ compared to previous studies, but ensures that we have a more inclusive assessment of the high-redshift SFGs.

4.2. Evolution with UV magnitude and Lyα luminosity

The corresponding Lyα luminosities and absolute UV magnitudes M_{1500} have been computed for all SFG in the three samples, including the magnification correction. Lyα luminosities are based on the observed Lyα fluxes and spectroscopic redshifts for Samples 1 and 3, and the limiting flux and photometric redshifts for Sample 2. Absolute magnitudes M_{1500} are based on

the observed SED fit and spectroscopic (Sample 1) or photometric (Sample 2) redshifts, and limiting magnitudes and spectroscopic redshifts for Sample 3. Figure 6 displays the distribution of the different populations of SFGs in terms of their observed and derived properties. This figure illustrates the effects of the magnification μ affecting each galaxy and also the impact of the limiting Lyα flux and m_{1500} values assigned to Samples 2 and 3, respectively. In the left panel of Fig. 6, the m_{1500} value has been recomputed based on the SED of each galaxy in Sample 1; for Sample 3, it is the limiting magnitude for each source as described above. The effect of magnification in spreading the distribution of galaxies towards the faintest luminosities is clearly seen in the right panel, which shows the Lyman α luminosity versus absolute UV magnitude M_{1500} after correction for magnification μ. As seen in this figure, given the limiting Lyα flux assigned to Sample 2, this population of pure LBGs tends to merge with the LBG + LAE population (Sample 1) for magnitudes $M_{1500} > -17$ to -16, with the precise value depending on the somewhat arbitrary flux limit adopted for the nondetection (see beginning of Sect. 4). The bulk of the galaxies in Sample 3 are distributed between $-16 < M_{1500} < -13$.

The main results of this study are summarized in Fig. 7, the central part of which shows the three samples in a plot presenting the Lyα luminosity in log-scale versus M_{1500}, in a similar way to in Fig. 6, with redshift color coded. Ultra-violet magnitude and Lyα luminosity histograms of the three samples are also provided on the side.

Regarding the SFR, Fig. 7 also displays the locus of the SFR$_{Ly\alpha}$ = SFR$_{uv}$ for a constant star-formation system. This relation was computed using the standard conversion in Kennicutt (1998) for SFR$_{Ly\alpha}$, and the common conversion also given in Kennicutt (1998) based on a Salpeter IMF for the SFR$_{uv}$. Since none of the values presented in Fig. 7 have been corrected for
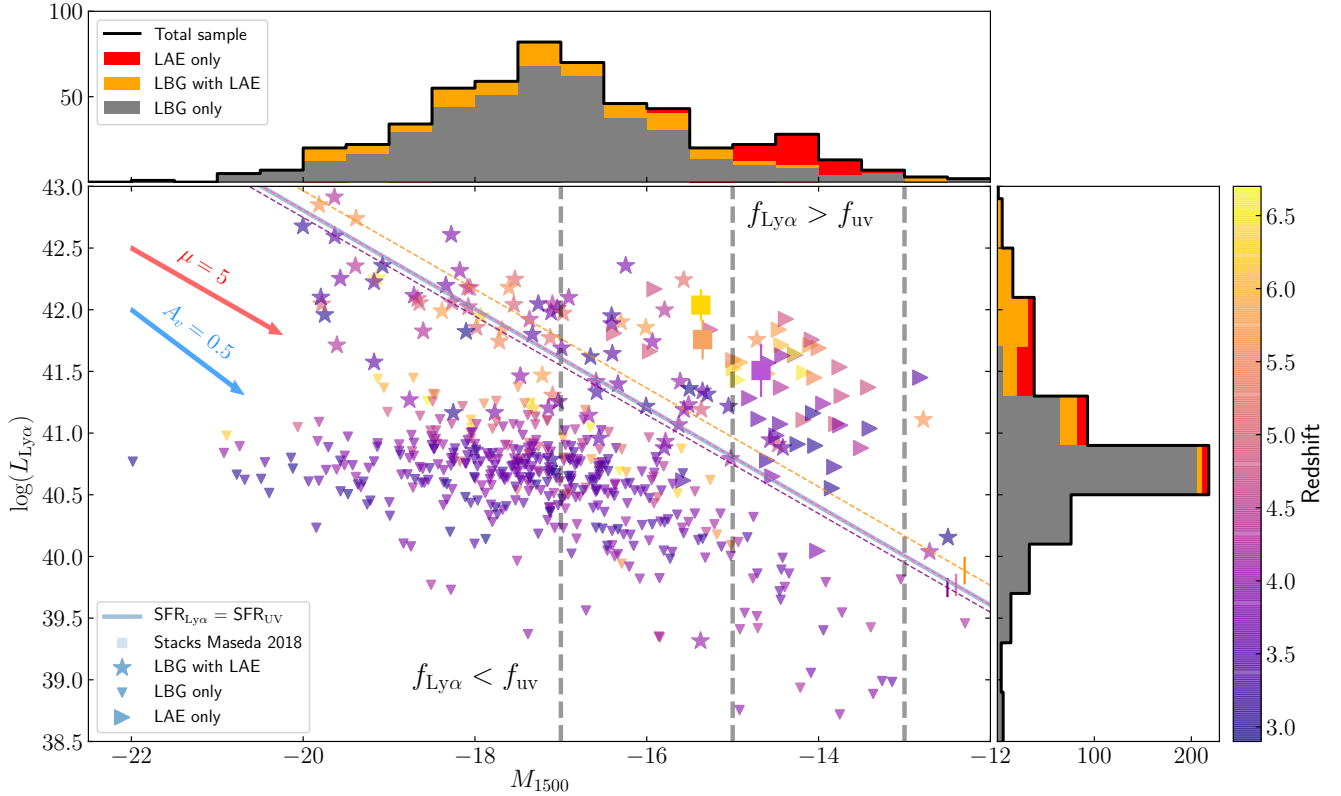
Fig. 7. Lyman α luminosity versus absolute UV magnitude, with redshift encoded in the color bar. On the top (right) are UV absolute magnitude (Lyα luminosity) histograms for the three samples, stacked on each other, using the same colors as in Fig. 4. Galaxies in Samples 2 and 3 have upper-limit estimations of their Lyα and UV fluxes (see text for details). All values have been corrected for magnification but not for possible dust extinction. The thick blue line displays the locus of the $SFR_{Ly\alpha} = SFR_{uv}$ for a constant star-formation system. The dashed violet, pink, and orange lines correspond to the best fit for the offset in this relation (with fixed slope) when the sample is split in the redshift bins: $2.9 < z < 4.0$, $4.0 < z < 5.0$, and $5.0 < z < 6.7$, respectively. Uncertainties on offset values are shown as vertical lines of the same color. The three vertical gray dashed lines correspond to $M_{1500} = -17$, $M_{1500} = -15$, $M_{1500} = -13$, which correspond roughly to the observational limit reached in blank fields, lensing fields, and the extrapolation needed to ensure that the UV LF provides enough ionizing flux for reionization (see Bouwens et al. 2015a). Red and blue arrows indicate the effect of a magnification factor of $\mu = 5$ and a reddening $A_V = 0.5$ magnitudes, respectively.

dust absorption, this constant star-formation line also represents the locus where the escape fraction for Lyα photons is the same as for UV photons ($f_{Ly\alpha} = f_{uv}$). Regarding the total ionizing flux density (or the SFR density, SFRD), this means that objects along this line yield the same values when measuring either the UV continuum or the Lyα line flux. Galaxies found above or below this line in this simple model have respectively $f_{uv} < f_{Ly\alpha}$ or $f_{uv} > f_{Ly\alpha}$. In addition, the scatter can be easily understood given the variety of star-forming regimes that are not fairly represented by stationary or constant star-formation regimes.

The three samples are each exploring different regions of Fig. 7. For bright galaxies with $M_{1500} < -15$, almost all SFGs in the present sample are selected as LBGs. However, for galaxies fainter than $M_{1500} = -15$ the proportion of SFGs only seen as LAEs progressively increases at lower UV luminosity. This result is in good agreement with the recent study of Maseda et al. (2018) which concluded that the LAE selection is better suited to identify and study intrinsically faint UV galaxies. This also suggests that the LAE LF is a better proxy of the SFG population when focusing on the faint end. The observed trend depends on the relative depth between MUSE and HST observations: deeper HST observations would increase the number of faint LBGs detected. Needless to say that such observations are extremely expensive and the HFF data are currently the deepest observations available.

In addition to the theoretical $SFR_{Ly\alpha} = SFR_{uv}$ locus, the same relation has been adjusted with the offset as a free parameter, keeping a constant slope, for galaxies in Sample 1 split in the following redshift bins: $2.9 < z < 4.0$ (43 sources), $4.0 < z < 5.0$ (27 sources), and $5.0 < z < 6.7$ (22 sources). The results are presented respectively by the dashed violet, pink, and orange lines in Fig. 7, where the derived uncertainties from the fit are represented as vertical error bars of the same color. Leaving this offset free means leaving the ratio $f_{Ly\alpha}/f_{UV}$ free in such a way that the fit can be seen as an average value of this ratio over the sample considered. For the two lower redshift bins, the adjusted line is fully consistent with the $SFR_{Ly\alpha} = SFR_{uv}$ locus within the 1σ level, whereas a $f_{Ly\alpha} > f_{uv}$ is observed for the higher redshift bin with a $\sim 1\sigma$ significance.

When looking at galaxies of Sample 1, on average, "bright" galaxies with $M_{1500} < -17$ tend to be under the $SFR_{Ly\alpha} = SFR_{uv}$ locus, therefore extending a trend already observed for brighter samples at such high redshifts (see e.g., Ando et al. 2006; Schaerer et al. 2011). Given the limiting detection levels in this survey, almost all galaxies in Sample 3 are located above the $SFR_{Ly\alpha} = SFR_{uv}$ locus, as well as the faintest galaxies of Sample 1 with $M_{1500} > -17$, in such a way that the number of galaxies with $SFR_{Ly\alpha} > SFR_{uv}$ at $M_{1500} > -17$ is larger than for $M_{1500} < -17$. Such a behavior could be explained by the evolution of the dust content, and the relative distribution of dust and

stars in star-forming regions, as discussed below. Also, the large scatter observed in Sample 1 for all three redshift bins could be representative of individual variation in the f_{Ly_α}/f_{UV} ratio related to the star formation regime, the age of the stellar population, the dust content, and the relative distribution of stars and dust.

It is worth emphasizing that the LBG sample used throughout this work is NIR-selected (i.e., selected based on the rest frame continuum at ~ 4000 Å down to 2000 Å for $z \sim 3-7$ respectively). We expect a systematic trend in the sense that LBG galaxies with extremely blue continuum could have been preferentially missed at $z \sim 3-4$ with respect to $z \sim 6-7$. While this certainly impacts the statistical significance of our analysis, this effect cannot account for the systematic trends presented above.

The fact that all SFGs with $M_{1500} < -17$ in the present sample are selected as LBGs is particularly interesting because this roughly corresponds to the observational limit of the deepest HST blank fields (see e.g., Bouwens et al. 2015a). This limit can be pushed as faint as $M_{1500} \sim -15$ in strong lensing fields before a significant correction is required to account for the contribution of LAEs without continuum detection. This means that the UV LF derived from LBG selection can be safely integrated down to $M_{1500} \sim -15$ to derive the total ionizing flux without including the additional contribution of the (pure) LAE population. Reaching down to $M_{1500} \sim -15$ up to $z \sim 7$ is only possible in lensing fields, as shown by different studies (see e.g., Livermore et al. 2017; Bouwens et al. 2017; Atek et al. 2018). The situation is different for $M_{1500} > -15$, as the pure LAE fraction among SFGs increases towards the faintest UV luminosities. As the M_{1500} values and associated luminosities for pure LAE galaxies are upper limits, it is not possible to determine individually whether or not they probe the same luminosity domain as (extremely faint) LBGs not detected as LAEs (Sample 2). Therefore, it is difficult to properly estimate the relative contribution to the ionizing flux for the ensemble of SFGs. For illustrative purposes, we provide an upper limit on the fraction of LAEs among all SFGs in the range $-15 \leq M_{1500} \leq -14$ where the completeness of the UV selection starts to drop. Using the lower limits on M_{1500} derived for Sample 3, the computed upper limit and $1 - \sigma$ values are $N(LAE)/N(SFG) = 0.42 \pm 0.14$.

Stacking the galaxies of Sample 3 in redshift bins following the technique adopted by Maseda et al. (2018) would provide further information about their average UV continuum, but this remains challenging because the strong variation of individual amplification makes it nontrivial to give similar weight to all stacked LAEs; also the sample of pure LAEs is still very small. Therefore, based on the present results it is still difficult to quantify the missing contribution of LAE to the ionizing flux density with respect to the extrapolation of the LBG-based UV LF to $M_{1500} \sim -13$, if any, up to $z \sim 7$.

For the sample of SFGs studied here, bright galaxies with $M_{1500} < -17$ tend to be under the $SFR_{Ly\alpha} = SFR_{uv}$ locus, whereas galaxies with $M_{1500} > -17$ are mostly observed above. Also, a higher $SFR_{Ly\alpha}$ (with respect to SFR_{uv}) is observed for galaxies at $z > 5$ as compared to $z < 5$ but, as discussed above, this effect is only at $\sim 1\sigma$ significance for this sample. Several effects combined together could explain the observations regarding the main trends and the scatter, including a genuine evolution in the f_{Ly_α}/f_{UV} ratio.

Possibly the simplest explanation for these trends is the age of the stellar populations. As previously suggested by Ando et al. (2006), if UV "bright" galaxies start their star-formation earlier than UV "faint" galaxies, they are expected to contain older stellar populations and be more chemically evolved and dustier, which could explain a relative decrease in their Lyα emission. Conversely, for $M_{1500} > -17$ galaxies, the presence of a younger

stellar population producing a harder spectrum with lower metallicity stars is expected to result in a the relative increase of the Lyα emission. This effect was also discussed in the past (see e.g., Erb et al. 2014). The original result here is that these effects are seen for very faint $M_{1500} \sim -15$ galaxies, much fainter than in previous studies. Regarding the scatter, even in the case of a constant SFR, the ratio of UV to Lyα luminosity produced by a young stellar population evolves and requires ~ 100 Myr before reaching the Kennicut equilibrium (Verhamme et al. 2008). The same is true in the case of a more realistic nonconstant and bursty SFR, which could explain part of the observed scatter.

Regarding the relative increase in $SFR_{Ly\alpha}$ with respect to SFR_{uv} for the faintest galaxies ($M_{1500} > -17$), an interesting explanation is the scenario described by Neufeld (1991), and also suggested by Atek et al. (2014), based on the existence of a multi-phase ISM with dust, where the Lyα emission is enhanced with respect to the nonresonant emission at similar wavelengths (i.e., UV continuum photons in the present case). Following this scenario, neutral gas and dust reside in clumps and they are surrounded by ionized medium. The Lyα photons are scattered away when reaching the surface of these clumps while the UV photons can penetrate inside where they are more easily absorbed by the dust. Therefore, even though $f_{Ly\alpha}$ decreases with increasing dust content or reddening, the ratio f_{Ly_α}/f_{UV} could increase because f_{uv} decreases faster than $f_{Ly\alpha}$ in the presence of dust clumps. Because faint UV galaxies tend to be less dusty and more clumpy than bright galaxies – as predicted by models (see e.g., Garel et al. 2012) – this effect is expected to preferentially impact the faintest population. Several previous studies have mentioned the importance of this mechanism (see e.g., Hayes et al. 2011, 2013; Atek et al. 2014; Matthee et al. 2016). However, as pointed out by Duval et al. (2014) based on their 3D Monte Carlo Lyα radiation transfer code, special conditions could be needed to have Lyα photons escaping more easily than the continuum (i.e., an almost static ISM, extremely clumpy, and very dusty). We do not have enough information to constrain the impact of this effect on our sample.

Geometrical effects are also important and certainly contribute to the observed scatter. A more uniform dust distribution makes the absorption of Lyα photons more likely, leading to $f_{uv} > f_{Ly\alpha}$, a systematic trend observed in the present sample for $M_{1500} < -17$ galaxies. Simulations by Verhamme et al. (2012), studying the effect of disk orientation, showed the dramatic effect of inclination on the Lyα observed properties (luminosity, EW and profile), with luminosity increasing from edge-on to face-on because of a smaller number of the resonant scattering; these effects being much stronger for Lyα photons than for the UV continuum. Observations by Shibuya et al. (2014a) of LAEs at $z \sim 2.2$ confirm this inclination trend. Several authors have pointed out the fact that the neutral hydrogen column density is a really important value affecting the Lyα emissivity (see e.g., Shibuya et al. 2014b; Hashimoto et al. 2015). For galaxies with the lower UV luminosities (likely the smaller masses), the observed relative excess in the f_{Ly_α} could be related to the fact that large gaseous disks are not yet in place, in addition to possible age effects, as mentioned above (see e.g., Erb et al. 2014).

Additional differential effects on the Lyα emissivity are expected from different physical conditions affecting the nebular regions, in particular the ionization states, if these regions are density- rather than ionization-bounded. Such effects have been described and considered by several authors when discussing the spectral signatures expected and observed for SFGs at high-z (see e.g., Zackrisson et al. 2013; Nakajima et al. 2016; Shibuya et al. 2019).

5. Conclusions

We studied the intersection between the LAE and the LBG population behind the HFF cluster A2744. Our findings can be summarized as follows:

- For faint UV-selected galaxies with $M_{1500} \geq -20.25$, the fraction of LAEs among SFGs increases with redshift up to $z \sim 6$ and decreases at $z \gtrsim 6$, in agreement with previous findings (see e.g., Arrabal Haro et al. 2018).
- As faint as $M_{1500} \sim -15$, the LBG population seems to provide a good representation of the total SFG population, in particular when computing the total ionizing flux in the volume explored by current surveys.
- The selection of Lyα emitters allows us to detect a population of intrinsically UV faint galaxies ($M_{1500} \geq -15$) with significant star formation (typically 0.01 to 0.1 $M_\odot$/yr) that are missed in present deep blank and lensing field LBG photometric surveys. In this respect, our results are in good agreement with those of Maseda et al. (2018). This also shows that when assessing the faint part of the population of SFGs with $M_{1500} \geq -15$ with the current deepest photometric data, a correction is needed to account for the contribution of the LAEs with no UV counterpart detection.

There is no clear evidence, based on the present results, for an intrinsic difference between the properties of the two populations selected as LBGs and/or LAEs. However, further investigation is needed. In particular, some systematic trends appear in the population selected as LBGs and LAEs in the sense that the UV-brightest galaxies seem to exhibit a smaller f_{Ly_α}/f_{UV} ratio, increasing towards the faintest luminosities. These trends, previously observed in other samples of SFGs at high-z (see e.g., Ando et al. 2006; Erb et al. 2014; Hashimoto et al. 2017), are seen here for very faint $M_{1500} \sim -15$ galaxies, much fainter than in previous studies. Several effects acting in combination could explain these differential trends, such as the age of the stellar populations, a different distribution of ISM and stars, geometrical effects, and physical conditions affecting the nebular regions. Measuring the UV slopes of these galaxies could provide additional information in this respect.

References

Ando, M., Ohta, K., Iwata, I., et al. 2006, ApJ, 645, L9
Arrabal Haro, P., Rodríguez Espinosa, J. M., Muñoz-Tuñón, C., et al. 2018, MNRAS, 478, 3740
Atek, H., Kunth, D., Schaerer, D., et al. 2014, A&A, 561, A89
Atek, H., Richard, J., Jauzac, M., et al. 2015, ApJ, 814, 69
Atek, H., Richard, J., Kneib, J.-P., & Schaerer, D. 2018, MNRAS, 479, 5184
Bacon, R., Accardo, M., Adjali, L., et al. 2010, Ground-based and Airborne Instrumentation for Astronomy III, 7735, 773508
Bacon, R., Conseil, S., Mary, D., et al. 2017, A&A, 608, A1
Bertin, E., & Arnouts, S. 1996, A&AS, 117, 393
Bolzonella, M., Miralles, J. M., & Pelló, R. 2000, A&A, 363, 476
Bouwens, R. J., Thompson, R. I., Illingworth, G. D., et al. 2004, ApJ, 616, L79
Bouwens, R. J., Illingworth, G. D., Oesch, P. A., et al. 2015a, ApJ, 811, 140
Bouwens, R. J., Illingworth, G. D., Oesch, P. A., et al. 2015b, ApJ, 803, 34
Bouwens, R. J., Oesch, P. A., Illingworth, G. D., Ellis, R. S., & Stefanon, M. 2017, ApJ, 843, 129
Bruzual, G., & Charlot, S. 2003, MNRAS, 344, 1000
Calzetti, D., Armus, L., Bohlin, R. C., et al. 2000, ApJ, 533, 682
Caruana, J., Wisotzki, L., Herenz, E. C., et al. 2018, MNRAS, 473, 30
Castellano, M., Amorín, R., Merlin, E., et al. 2016, A&A, 590, A31
Chabrier, G. 2003, PASP, 115, 763
Coleman, G. D., Wu, C.-C., & Weedman, D. W. 1980, ApJS, 43, 393
Dayal, P., & Ferrara, A. 2012, MNRAS, 421, 2568
De Barros, S., Pentericci, L., Vanzella, E., et al. 2017, A&A, 608, A123
de La Vieuville, G., Bina, D., Pello, R., et al. 2019, A&A, 628, A3
Duval, F., Schaerer, D., Östlin, G., & Laursen, P. 2014, A&A, 562, A52
Erb, D. K., Steidel, C. C., Trainor, R. F., et al. 2014, ApJ, 795, 33
Finkelstein, S. L., Ryan Russell, E., Papovich, C., et al. 2015, ApJ, 810, 71
Garel, T., Blaizot, J., Guiderdoni, B., et al. 2012, MNRAS, 422, 310
Garel, T., Guiderdoni, B., & Blaizot, J. 2016, MNRAS, 455, 3436
Hashimoto, T., Verhamme, A., Ouchi, M., et al. 2015, ApJ, 812, 157
Hashimoto, T., Garel, T., Guiderdoni, B., et al. 2017, A&A, 608, A10
Hayes, M., Schaerer, D., Stlin, G., et al. 2011, ApJ, 730, 8
Hayes, M., Östlin, G., Schaerer, D., et al. 2013, ApJ, 765, L27
Hayes, M., Östlin, G., Schaerer, D., et al. 2015, IAU General Assembly, 29, 2256902
Inami, H., Bacon, R., Brinchmann, J., et al. 2017, A&A, 608, A2
Jullo, E., & Kneib, J. P. 2009, MNRAS, 395, 1319
Jullo, E., Kneib, J. P., Limousin, M., et al. 2007, New J. Phys., 9, 447
Kennicutt, R. C., Jr 1998, ApJ, 498, 541
Kinney, A. L., Calzetti, D., Bohlin, R. C., et al. 1996, ApJ, 467, 38
Kneib, J.-P., Ellis, R. S., Smail, I., Couch, W. J., & Sharples, R. M. 1996, ApJ, 471, 643
Kusakabe, H., Blaizot, J., Garel, T., et al. 2020, A&A, 638, A12
Leclercq, F., Bacon, R., Wisotzki, L., et al. 2017, A&A, 608, A8
Leitherer, C., Schaerer, D., Goldader, J. D., et al. 1999, ApJS, 123, 3
Livermore, R. C., Finkelstein, S. L., & Lotz, J. M. 2017, ApJ, 835, 113
Lotz, J. M., Koekemoer, A., Coe, D., et al. 2017, ApJ, 97,
Mahler, G., Richard, J., Clément, B., et al. 2018, MNRAS, 692, 663
Maseda, M. V., Bacon, R., Franx, M., et al. 2018, ApJ, 865, L1
Matthee, J., Sobral, D., Oteo, I., et al. 2016, MNRAS, 458, 449
McLure, R. J., Cirasuolo, M., Dunlop, J. S., Foucaud, S., & Almaini, O. 2009, MNRAS, 395, 2196
McLure, R. J., Dunlop, J. S., Bowler, R. A. A., et al. 2013, MNRAS, 432, 2696
Merlin, E., Amorín, R., Castellano, M., et al. 2016, A&A, 590, A30
Nagamine, K., Ouchi, M., Springel, V., & Hernquist, L. 2010, PASJ, 62, 1455
Nakajima, K., Ellis, R. S., Iwata, I., et al. 2016, ApJ, 831, L9
Neufeld, D. A. 1991, ApJ, 370, L85
Oesch, P. A., Stiavelli, M., Carollo, C. M., et al. 2007, ApJ, 671, 1212
Oke, J. B., & Gunn, J. E. 1983, ApJ, 266, 713
Orsi, Á., Padilla, N., Groves, B., et al. 2014, MNRAS, 443, 799
Pelló, R., Hudelot, P., Laporte, N., et al. 2018, A&A, 620, A51
Pentericci, L., Fontana, A., Vanzella, E., et al. 2011, ApJ, 743, 132
Piqueras, L., Conseil, S., Shepherd, M., et al. 2017, ArXiv e-prints [arXiv:1710.03554]
Schaerer, D., de Barros, S., & Stark, D. P. 2011, A&A, 536, A72
Schenker, M. A., Ellis, R. S., Konidaris, N. P., & Stark, D. P. 2014, ApJ, 795, 20
Shapley, A. E. 2011, ARA&A, 49, 525
Shibuya, T., Ouchi, M., Harikane, Y., & Nakajima, K. 2019, ApJ, 871, 164
Shibuya, T., Ouchi, M., Nakajima, K., et al. 2014a, ApJ, 788, 74
Shibuya, T., Ouchi, M., Nakajima, K., et al. 2014b, ApJ, 785, 64
Stark, D. P., Ellis, R. S., & Ouchi, M. 2011, ApJ, 728, L2
Steidel, C. C., Adelberger, K. L., Shapley, A. E., et al. 2003, ApJ, 592, 728
Steidel, C. C., Bogosavljević, M., Shapley, A. E., et al. 2018, ApJ, 869, 123
Tilvi, V., Papovich, C., Finkelstein, S., et al. 2014, ApJ, 794, 5
Treu, T., Schmidt, K. B., Trenti, M., Bradley, L. D., & Stiavelli, M. 2013, ApJ, 775, L29
Verhamme, A., Schaerer, D., Atek, H., & Tapken, C. 2008, A&A, 491, 89
Verhamme, A., Dubois, Y., Blaizot, J., et al. 2012, A&A, 546, A111
Wisotzki, L., Bacon, R., Brinchmann, J., et al. 2018, Nature, 562, 229
Zackrisson, E., Inoue, A. K., & Jensen, H. 2013, ApJ, 777, 39